Snapshot Hyperspectral Imaging using Petrographic Thin Section

Yuta Fujimoto
NAIST
Ikoma, Nara 630-0192, Japan

Kazuya Kitano
NAIST
kitano.kazuya@is.naist.jp

Kazuma Fujiwara
NAIST

Yuki Fujimura
NAIST

Takuya Funatomi
NAIST

Yasuhiro Mukaigawa
NAIST

Abstract

In this study, we propose a novel snapshot hyperspectral imaging method using a rock filter consisting of a petrographic thin section between two linear polarizers. There is no need to use a complex process on the scale of several micrometers or smaller to fabricate the spectral sensor, as this can be achieved by using power tools. Rock filter works as a spatial-spectral filter. After encoding the spectral information in the scene using rock filter, the spectral distribution is decoded by solving an optimization problem, and a spectral image can be reconstructed. Through simulations reconstructing the spectra of LED lights, we evaluate reconstruction accuracy when the patterns and spatial resolution are changed. Furthermore, we demonstrate that hyperspectral imaging is feasible when a colorchecker is used as a target in a real environment.

1 Introduction

Hyperspectral imaging is a technology that acquires the intensity distribution for each wavelength of light, enabling the extraction of richer features from scenes that are difficult to distinguish using human perception or standard RGB cameras. Applications of hyperspectral imaging include food inspection, crop growth monitoring, and mineral exploration [3, 8, 13].

General hyperspectral imaging methods include line-scan method and snapshot method [5]. In the line-scan method, a linear region is extracted through a slit, light is dispersed in the wavelength direction using a diffraction grating or prism, and it is projected onto a two-dimensional sensor. This method enables high-resolution acquisition of spatial-spectral cubes but has drawbacks such as complex and expensive optical systems and long acquisition times, which limit its range of applications.

In contrast, snapshot hyperspectral imaging methods can acquire spatial–spectral cubes in a single shot, enabling faster measurements than the line-scan method [2]. Among these, methods using spatial-spectral filters [24, 19, 25, 23, 21, 22] achieve hyperspectral imaging with a simple optical system consisting of
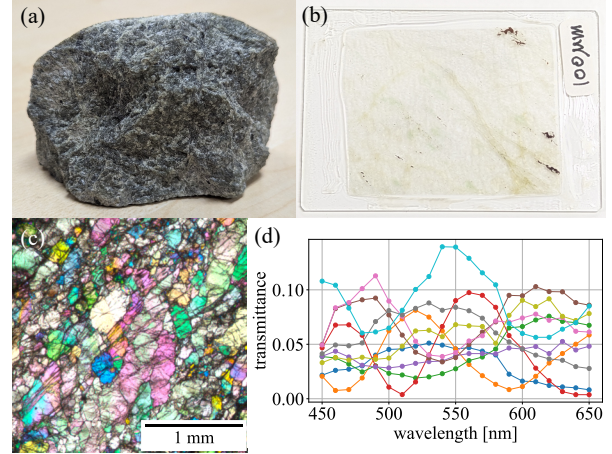

Figure 1: Overview of rock filter. Among many rocks, we chose lherzolite as a rock filter composition. (a) Lherzolite before slicing. (b) Petrographic thin section cut to a thickness of 100 μm. (c) Psuedo-color image of rock filter. (d) Spectral transmittance samples in (c).

only a single filter and a camera by encoding spectral information in the scene. However, the filters used in existing studies require microfabrication technology on the scale of several micrometers or smaller, including photolithography, which requires expensive and large machinery and clean rooms.

Thin petrographic sections are used mainly in the field of petrology to investigate the formation process of rocks by identifying the minerals they contain and observing their important textures [20]. One of the analytical methods used is the identification of minerals using a polarizing microscope, which utilizes the birefringence properties of minerals. This mineral-induced birefringence has the potential for application as an optical filter. For example, Sasaki *et al.* [17] proposed a depolarization filter using calcite. Moreover, minerals can serve as spectral filters utilizing birefringence properties such as waveplate [15], LCVR [1], and spatial light modulator [16].

In this study, we propose a novel hyperspectral imaging method using a *rock filter*, which consists of a
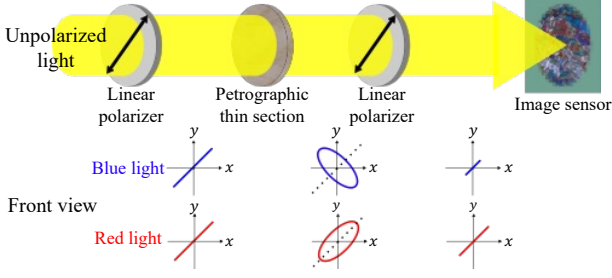
Figure 2: Encoding process of rock filter.

petrographic thin section between two linear polarizers (Fig. 1). Petrographic thin sections can be fabricated using general power tools [4, 14], such as diamond cutters and polishing machines, without the need for special equipment such as semiconductor manufacturing apparatus and clean rooms. Rock filters have a lower border of manufacturing.

2 Method

Figure 2 illustrates the encoding process of the rock filter. First, unpolarized incident light passes through the first linear polarizer, and becomes linearly polarized. Subsequently, the petrographic thin section which has birefringence properties generates phase retardation, resulting in the conversion of linear polarization to elliptical polarization. The phase retardation is determined by the birefringence of the minerals at the position of the petrographic thin section x, its thickness, and the wavelength of light λ [7]. The phase retardation determines the degree of circular polarization, and it affects the intensity of light passing through the second linear polarizer. This model is the same as the conventional spectral filters utilizing birefringence properties [15, 1, 16]. Consequently, the spectral transmittance of rock filter $t(x, \lambda)$ also becomes sinusoidal waves along the spectral axis [12], as shown in Fig. 1(d). However, it is difficult to completely model the spectral transmittance of rock filter because rock filter is made of naturally occurring rocks. To reconstruct the spectral image, its measurement is required, and we calibrated it using a monochromator, as explained later in Sec. 3.

Assuming a spectral distribution in the scene $s(x, \lambda)$, the encoded spectral measurement $i(x)$ is expressed as

$$i(x) = \sum_\lambda s(x, \lambda) \ t(x, \lambda). \quad (1)$$

Reconstructing a spectral image from a single encoded spectral measurement is an ill-posed problem, and the solution is not uniquely determined. Therefore, $N \times N$ pixels on the sensor are grouped into a patch $\mathcal{X}_p$, and the spectra in the patch are assumed to be uniform. Using all pixels $x \in \mathcal{X}_p$, the spectral distribution $s(\mathcal{X}_p, \lambda)$
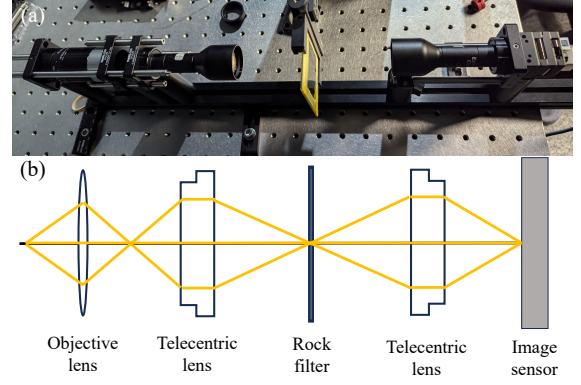

Figure 3: (a) Implemented optics system. (b) Optical diagram of the system.

Table 1: PSNR (in dB) of each estimated LED spectrum in Fig. 5(b).

filters	Blue	Green	Red
rock filter (2×2)	17.5	14.1	16.0
rock filter (8×8)	32.0	30.2	42.8
rock filter (32×32)	51.0	35.7	46.2
RGB	21.9	13.7	17.7
10 waveplates [15]	27.8	17.7	24.3

is estimated by solving the following optimization problem,

$$\hat{s}(\mathcal{X}_p, \lambda) =$$
$$\underset{s \geq 0}{\mathrm{argmin}} \left\{ \sum_{x \in \mathcal{X}_p} \left(i(x) - \sum_\lambda s(\mathcal{X}_p, \lambda) \ t(x, \lambda) \right)^2 + \alpha \left\| \nabla_\lambda^2 \ s(\mathcal{X}_p, \lambda) \right\|_2^2 \right\}. \quad (2)$$

Here, we use a spectral smoothness prior as a regularization term as well as a non-negativity constraint. Since the spectral transmittance of the rock filter is non-uniform, as long as the assumption of having uniform spectra within the patch is valid, the spectral image reconstruction accuracy improves as the patch size increases.

3 Hardware Implementation

We used a thin section of lherzolite as a rock filter composition among many rocks due to the significant variation in birefringence exhibited by the compositions of lherzolite, which include olivine, orthopyroxene, and clinopyroxene [9].

Figure 3 shows the optical system for real environment verification. Because we could not remove the glass filter on the image sensor and combine it with the rock filter, as Zhao *et al.* [26] did, we used a relay system. We used a 50 mm f/2.4–16 objective lens
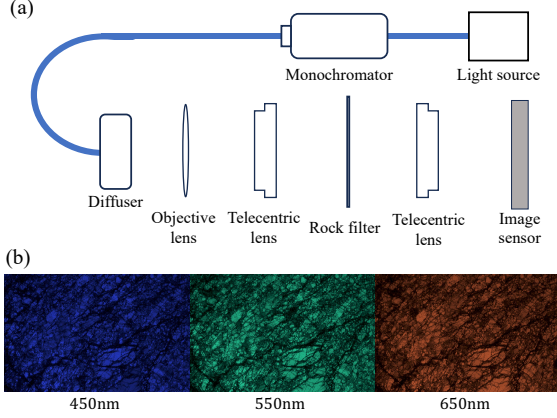
Figure 4: Calibration setup. (a) Optical diagram of the calibration system. Monochromatic light from a light source is selected by a monochromator and passed through a diffuser for uniform illumination. (b) Measured images for the wavelength of 450 nm, 550 nm, and 650 nm.
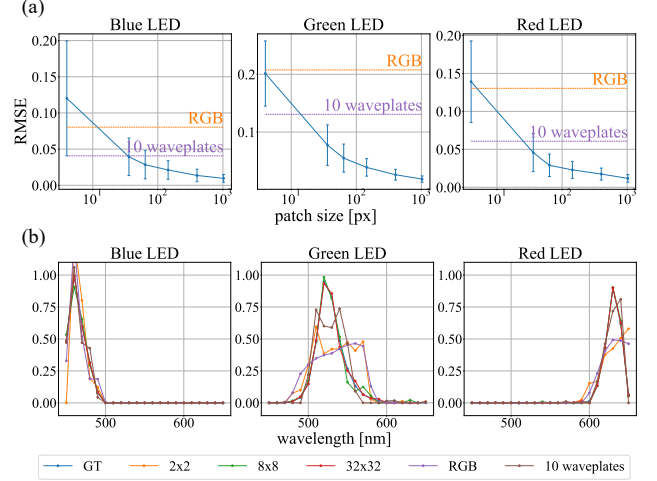

Figure 5: Estimation results of LED lights spectra in the simulation experiment. (a) RMSE for each patch size $N \times N$. (b) Comparison of estimated LED spectra with ground truth.

(FUJINON HF50XA-5M), two 65 mm f/9 0.5X telecentric lenses (Edmund Optics WD CompactTL$^{\mathrm{TM}}$), and a 4096×2160 pixels 3.45 µm pixel pitch CMOS image sensor (LUCID PHX089S-CC). The petrographic thin section is a 100 µm thick lherzolite from Horoman in Hokkaido, Japan, fixed using soda glass and optical adhesive. The thicker the petrographic thin section, the greater the range of phase retardation, and it may lead to higher spectral diversity. However, if it is too thick, the color of the rock itself will affect the rock filter and make it harder for the incident light to pass through. We chose this thickness to balance this out.

For the measurement of spectral transmittance $t(x, \lambda)$, a monochromator (Optometrics Manual Mini-Chrom Monochromator) and a xenon lamp (Ocean Optics HPX-2000 Xenon Light Source) were used (Fig. 4).

4 Simulation Experiment

The spectral transmittance of the rock filter is spatially non-uniform, and the reconstruction accuracy depends on the pattern of the rock and the patch size $N \times N$. Therefore, we obtained overlapped 170 patches from the measured spectral transmittance data while changing the patch size from 2×2 to 32×32 and estimated the spectral image in the scene with an ideally uniform spectrum on simulation. The scene spectra are three types of LED lights from Thorlabs: red (630 nm LIU630A), blue (470 nm LIU470A), and green (525 nm LIU525B). In the experiment, 21 bands were reconstructed with a resolution of 10 nm in the range of 450 nm to 650 nm. When creating the encoded spectral measurements from the spectral images and the spectral transmittance of the rock filter, we added random noise following a Gaussian distribution with a standard deviation of 2 %.

Figure 5(a) shows the change in root mean squared error (RMSE) with respect to the number of pixels in a patch, presented as an error plot with standard deviation for all samples. For comparison, we used RGB Bayer pattern and polarization-induced spectral filters using waveplates (10 shots) [15]. On the condition scene is ideally uniform, the reconstruction using these filters can also be done using Eq. (2). Since the particle size of the petrographic thin section is larger than the pixel size of the image sensor, it is confirmed that when the number of pixels in a patch is small (around 2×2), the spatial diversity of the spectral transmittance in the rock filter is low, resulting in RMSE comparable to that of not using the rock filter. Additionally, the petrographic thin section contains grain boundaries, and the spectral transmittance becomes almost zero depending on the angle between this plane and the petrographic thin section. This results in incomplete encoding and, in some cases, worse reconstruction accuracy compared to the RGB Bayer pattern. On the other hand, increasing the number of pixels in a patch improves the diversity of the spectral transmittance and reduces the reconstruction error. Specifically, when the number of pixels reaches approximately 8×8, the error decreases to below that of 10 measurements taken by polarization-induced spectral filters using waveplates. Additionally, Fig. 5(b) shows the comparison results of the estimated spectra, and Table 1 shows peak signal-to-noise ratio (PSNR) of each estimated spectrum. It can be seen that when the patch size is larger than 8×8 pixels, the LED spectra are estimated almost correctly.
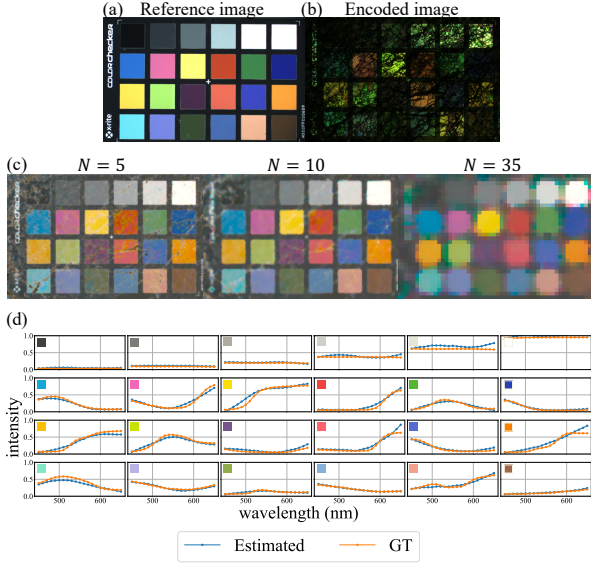
Figure 6: Estimation results of the spectral reflectance of colorchecker in the real experiment. (a) Reference image. (b) Encoded spectral measurement (1900px × 1200px). (c) Psuedo-color image of estimated hyperspectral images for N. These images are synthesized by an open-source Python package for colour science [11]. (d) Comparison of sample spectra in each color patch for $N = 35$ within estimation and ground truth.

Table 2: PSNR (in dB) and SAM (in degree) of estimated color patches for each patch size in Fig. 6(c).

patch sizes	PSNR	SAM
5×5	22.5	9.6
10×10	24.1	7.5
35×35	25.8	5.9

5 Real Experiment

Next, real environment verification was conducted using a colorchecker (X-Rite ColorChecker Passport Photo 2) as the target (Fig. 6). The illumination spectrum was estimated using a gray balance target (X-Rite ColorChecker Passport Photo 2). It was also used for the spatial alignment of spectral transmittance data to an encoded spectral measurement. After the optimization, median filter of kernel size 3×3 was applied to each reconstructed band image for noise suppression. Patch sizes were set to 5×5, 10×10, and 35×35. Figure 6(a) shows pseudo-color images of the estimated spectral images for each patch size, and Table 2 shows PSNR and spectral angular mapper (SAM) of all color patches. The results confirm that increasing the patch size improves the estimation accuracy within the color patches. However, for the 'colorchecker' text written in white on the left side of the colorchecker, reducing the patch size enables better recognition of the text. Patch

size should be adjusted to the target object. Furthermore, Fig. 6(d) shows a comparison between the estimated and ground truth spectra for each patch when the patch size is 35×35. It can be seen that the spectral reflectance is estimated approximately correctly for all patches.

6 Limitation

We exploit the microstructure of lherzolite, which has inherent variability, and it leads to inconsistent reconstruction performance. However, by avoiding thick grain boundaries, excessive performance degradation can be avoided.

7 Conclusion

In this study, we propose a novel snapshot hyperspectral imaging method using rock filter. Rock filter does not require complex manufacturing apparatus because the microstructure of rocks itself is a natural product of the Earth's interior. This characteristic can contribute to simpler manufacturing machinery and environment. The measurement of its spectral transmittance and the results of the simulation experiment demonstrate that the rock filter exhibits a high diversity in spectral transmittance. Experimental results confirm that the spectral image can be reconstructed accurately using the rock filter in a real environment.

Future work includes improving the performance of the spatial-spectral resolution and developing a more compact optical system. Although this study used lherzolite for validation, there may be other petrographic thin sections with smaller grain sizes and richer variations in birefringence. In addition, the combination of a rock filter with other optical elements, such as lens arrays [10] and Kaleidoscopic Imaging [6, 18], could be explored. Due to the non-uniform spectral transmittance of the rock filter, duplicating the scene changes the encoding pattern, potentially enabling more efficient reconstruction. Furthermore, the implemented optical system is bulky compared to other spatial-spectral filters. By removing the glass filter on the image sensor and integrating it with the rock filter, the optical system can be as compact as other systems.

References

[1] I. August, Y. Oiknine, M. AbuLeil, I. Abdulhalim, and A. Stern. Miniature compressive ultra-spectral imaging system utilizing a single liquid crystal phase retarder. *Scientific reports*, 6(1):1–9, 2016.

[2] K. Ding, M. Wang, M. Chen, X. Wang, K. Ni, Q. Zhou, and B. Bai. Snapshot spectral imaging: from spatial-spectral mapping to metasurface-based imaging. *Nanophotonics*, 13(8):1303–1330, 2024.

[3] A. A. Gowen, C. P. O'Donnell, P. J. Cullen, G. Downey, and J. M. Frias. Hyperspectral imaging–an emerging process analytical tool for food quality and safety control. *Trends in food science & technology*, 18(12):590–598, 2007.

[4] G. Grundmann and H. Scholz. Preparation methods in mineralogy & geology: the preparation of thin sections, polished sections, acetate foil prints. *preparation for elutriation analysis, and staining tests for the optical and electron microscopy.(2015) https://doi. org/10.13140/RG*, 2(2593.9360), 2015.

[5] N. Hagen and M. W. Kudenov. Review of snapshot spectral imaging technologies. *Optical Engineering*, 52(9):090901–090901, 2013.

[6] J. Y. Han and K. Perlin. Measuring bidirectional texture reflectance with a kaleidoscope. *ACM Trans. Graph.*, 22(3):741–748, July 2003.

[7] E. Hecht. *Optics*, chapter 8. Pearson, 2012.

[8] L. W. Lass, T. S. Prather, N. F. Glenn, K. T. Weber, J. T. Mundt, and J. Pettingill. A review of remote sensing of invasive weeds and example of the early detection of spotted knapweed (centaurea maculosa) and babysbreath (gypsophila paniculata) with a hyperspectral sensor. *Weed Science*, 53(2):242–251, 2005.

[9] M. Le Bas and A. L. Streckeisen. The IUGS systematics of igneous rocks. *Journal of the Geological Society*, 148(5):825–833, 1991.

[10] A. Manakov, J. Restrepo, O. Klehm, R. Hegedus, E. Eisemann, H.-P. Seidel, and I. Ihrke. A reconfigurable camera add-on for high dynamic range, multispectral, polarization, and light-field imaging. *ACM Transactions on Graphics*, 32(4):47–1, 2013.

[11] T. Mansencal, M. Mauderer, M. Parsons, N. Shaw, K. Wheatley, S. Cooper, J. D. Vandenberg, L. Canavan, K. Crowson, O. Lev, K. Leinweber, S. Sharma, T. J. Sobotka, D. Moritz, M. Pppp, C. Rane, P. Eswaramoorthy, J. Mertic, B. Pearlstine, M. Leonhardt, O. Niemitalo, M. Szymanski, M. Schambach, S. Huang, M. Wei, N. Joywardhan, O. Wagih, P. Redman, J. Goldstone, and S. Hill. Colour 0.3.16, Jan. 2020.

[12] S. A. Nelson. Interference phenomena, compensation, and optic sign. *Tulane Univ. Mineral*, pages 1–19, 2014.

[13] S. Peyghambari and Y. Zhang. Hyperspectral remote sensing in lithological mapping, mineral exploration, and environmental geology: an updated review. *Journal of Applied Remote Sensing*, 15(3):031501–031501, 2021.

[14] F. S. Reed and J. L. Mergner. Preparation of rock thin sections. *American Mineralogist: Journal of Earth and Planetary Materials*, 38(11-12):1184–1203, 1953.

[15] K. Salesin, D. Seyb, S. Friday, and W. Jarosz. Diy hyperspectral imaging via polarization-induced spectral filters. In *2022 IEEE International Conference on Computational Photography (ICCP)*, pages 1–12. IEEE, 2022.

[16] V. Saragadam, V. Rengarajan, R. Tadano, T. Zhuang, H. Oyaizu, J. Murayama, and A. C. Sankaranarayanan. Programmable spectral filter arrays using phase spatial light modulators. In *2023 IEEE International Conference on Computational Photography (ICCP)*, pages 1–12. IEEE, 2023.

[17] S. Sasaki, M. Udono, and Y. Koike. Random depolarization film design for real-color displays. *Applied optics*, 61(3):669–675, 2022.

[18] T. Takatani, T. Aoto, and Y. Mukaigawa. One-shot hyperspectral imaging using faced reflectors. In *Proceedings of the IEEE Conference on Computer Vision and Pattern Recognition*, pages 4039–4047, 2017.

[19] Z. Wang, S. Yi, A. Chen, M. Zhou, T. S. Luk, A. James, J. Nogan, W. Ross, G. Joe, A. Shahsafi, et al. Single-shot on-chip spectral sensors based on photonic crystal slabs. *Nature communications*, 10(1):1020, 2019.

[20] J. D. Winter. *Principles of igneous and metamorphic petrology*, volume 2, chapter 3. Pearson education Harlow, UK, 2014.

[21] X. Wu, D. Gao, Q. Chen, and J. Chen. Multispectral imaging via nanostructured random broadband filtering. *Optics Express*, 28(4):4859–4875, 2020.

[22] Z. Wu, Z. Zhang, Y. Xu, Y. Zhai, C. Zhang, B. Wang, and Q. Wang. Random color filters based on an all-dielectric metasurface for compact hyperspectral imaging. *Optics Letters*, 47(17):4548–4551, 2022.

[23] T. Xu, Y.-K. Wu, X. Luo, and L. J. Guo. Plasmonic nanoresonators for high-resolution colour filtering and spectral imaging. *Nature communications*, 1(1):59, 2010.

[24] M. Yako, Y. Yamaoka, T. Kiyohara, C. Hosokawa, A. Noda, K. Tack, N. Spooren, T. Hirasawa, and A. Ishikawa. Video-rate hyperspectral camera based on a cmos-compatible random array of fabry–pérot filters. *Nature Photonics*, 17(3):218–223, 2023.

[25] J. Yang, K. Cui, X. Cai, J. Xiong, H. Zhu, S. Rao, S. Xu, Y. Huang, F. Liu, X. Feng, et al. Ultraspectral imaging based on metasurfaces with freeform shaped meta-atoms. *Laser & Photonics Reviews*, 16(7):2100663, 2022.

[26] Y. Zhao, H. Guo, Z. Ma, X. Cao, T. Yue, and X. Hu. Hyperspectral imaging with random printed mask. In *Proceedings of the IEEE/CVF Conference on Computer Vision and Pattern Recognition*, pages 10149–10157, 2019.